Molecular intercalation in the van der Waals antiferromagnets $FePS_3$ and $NiPS_3$

Cong Li,[1,*] Ze Hu,[1,*] Xiaofei Hou,[2,*] Sheng Xu,[1] Zhanlong Wu,[1] Kefan Du,[1] Shuo Li,[1] Xiaoyu Xu,[1] Ying Chen,[1] Zeyu Wang,[3] Tiancheng Mu,[3] Tian-Long Xia,[1,4,†] Yanfeng Guo,[2,5,‡] B. Normand,[6,7] Weiqiang Yu,[1,4,§] and Yi Cui[1,4,‖]

[1]*Department of Physics and Beijing Key Laboratory of Opto-electronic Functional Materials & Micro-nano Devices, Renmin University of China, Beijing, 100872, China*

[2]*School of Physical Science and Technology, ShanghaiTech University, Shanghai, 201210, China*

[3]*Department of Chemistry, Renmin University of China, Beijing, 100872, China*

[4]*Key Laboratory of Quantum State Construction and Manipulation (Ministry of Education), Renmin University of China, Beijing, 100872, China*

[5]*ShanghaiTech Laboratory for Topological Physics, Shanghai, 201210, China*

[6]*Laboratory for Theoretical and Computational Physics, Paul Scherrer Institute, CH-5232 Villigen-PSI, Switzerland*

[7]*Institute of Physics, Ecole Polytechnique Fédérale de Lausanne (EPFL), CH-1015 Lausanne, Switzerland*

(Received 3 March 2024; accepted 19 April 2024; published 3 May 2024)

We have performed electrochemical treatment of the van der Waals antiferromagnetic materials $FePS_3$ and $NiPS_3$ with the ionic liquid EMIM-BF_4, achieving significant molecular intercalation. Mass analysis of the intercalated compounds, $EMIM_x$-$FePS_3$ and $EMIM_x$-$NiPS_3$, indicated respective intercalation levels, x, of approximately 27% and 37%, and x-ray diffraction measurements demonstrated a massive (over 50%) enhancement of the c-axis lattice parameters. To investigate the consequences of these changes for the magnetic properties, we performed magnetic susceptibility and ^{31}P nuclear magnetic resonance (NMR) studies of both systems. For $EMIM_x$-$FePS_3$, intercalation reduces the magnetic ordering temperature from $T_N = 120$ to 78 K, and we find a spin gap in the antiferromagnetic phase that drops from 45 to 30 K. For $EMIM_x$-$NiPS_3$, the ordering temperature is almost unaffected (changing from 148 to 145 K), but a change towards nearly isotropic spin fluctuations suggests an alteration of the magnetic Hamiltonian. Such relatively modest changes, given that the huge extension of the c axes is expected to cause a very strong suppression any interlayer interactions, point to the conclusion that the magnetic properties of both parent compounds are determined almost exclusively by two-dimensional (2D), intralayer physics. The changes in transition temperatures and low-temperature spin dynamics in both compounds therefore indicate that intercalation also results in a significant modulation of the intralayer magnetic interactions, which we propose is due to charge doping and localization on the P sites. Our study offers chemical intercalation with ionic liquids as an effective method to control not only the interlayer but also the intralayer interactions in quasi-2D magnetic materials.

DOI: 10.1103/PhysRevB.109.184407

I. INTRODUCTION

Low-dimensional magnetic systems have played a pivotal role not only in advancing our understanding of the quantum properties of materials but also in the realization and exploration of new concepts in many-body physics. Still, with the exception of certain geometrically discretized or strong-frustration scenarios, which lead to quantum disordered magnetic states including quantum spin liquids, most three-dimensional (3D) magnetic systems exhibit long-ranged order. Conversely, as emphasized by Bethe in his seminal work, low dimensions amplify quantum fluctuations and destabilize the conventional order parameters [1]. In the case of layered compounds, increasing the interlayer spacing by the insertion of large molecules is a very literal means of modulating the dimensionality, and hence the properties, from potentially 3D towards the 2D limit [2,3]. The discovery of 2D magnetic materials suitable for this type of control would hold significant promise for applications in nanoelectronics and spintronics [4].

For this reason, magnetic van der Waals materials have attracted extensive attention in recent years [5], although efforts at dimensional manipulation have so far been limited largely to approaching the monolayer limit by exfoliation. In this context, the Ising-type van der Waals magnets $Cr_2Ge_2Te_6$ and CrI_3 exhibit the emergence of intrinsic ferromagnetism with a high transition temperature in few- or monolayer films [6–8]; in particular, CrI_3 shows a systematic evolution of the ordering temperature and even the type of magnetic order with the number of layers [7]. $MnSe_2$ remains ferromagnetic (FM) at room temperature in its monolayer form [9], and most surprisingly room-temperature FM order emerges in monolayer VSe_2 despite the bulk material being paramagnetic [10].

*These authors contributed equally to this work.
†tlxia@ruc.edu.cn
‡guoyf@shanghaitech.edu.cn
§wqyu_phy@ruc.edu.cn
‖cuiyi@ruc.edu.cn

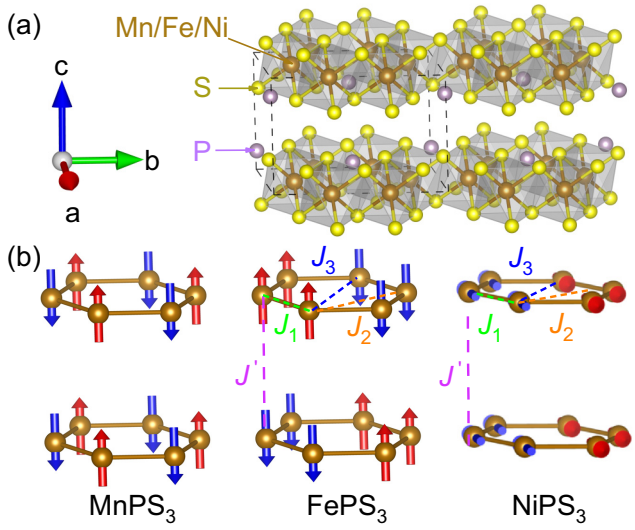

FIG. 1. Lattice and magnetic structure of MPS_3. (a) Crystal structure. The figure illustrates two unit cells containing eight MPS_3 units. (b) Magnetic structure below T_N. In $FePS_3$ and $NiPS_3$, J_1, J_2, and J_3 label respectively magnetic interactions between nearest-, next-nearest-, and next-next-nearest-neighbor sites; in both systems, the competition of $J_1 < 0$ and $J_3 > 0$ determines the zigzag magnetic structure. J' labels the interlayer interaction, which we note corresponds to ABC stacking of the magnetic ions in the honeycomb layers, and is AFM in $FePS_3$ but effectively ferromagnetic in $NiPS_3$. Blue and red arrows illustrate the relative orientations of local moments in the ordered phases.

The transition-metal trisulfide MPS_3 (M = Mn, Fe, Co, Ni) is a class of antiferromagnetic (AFM) van der Waals materials that has also been studied extensively [11–16]. As Fig. 1(a) shows, the MPS_3 compounds are isostructural, with the magnetic ions (M^{2+}) forming a honeycomb lattice. All exhibit the characteristics of a Mott insulator, displaying high resistivity at room temperature and a band gap well in excess of 1 eV (1.5 eV for $FePS_3$ and 1.6 eV for $NiPS_3$). This gap varies widely on exfoliation, offering an optoelectronic response over a broad frequency range for device applications [15]. $MnPS_3$ shows a technologically relevant nonreciprocal response arising from $\mathcal{PT}$ symmetry [17], $FePS_3$ exhibits a phase transition under pressure from insulating to metallic [18], and $NiPS_3$ in its AFM phase has coherent excitonic states [19].

Differences in the trigonal distortion of the MS_6 octahedra and in spin-orbit coupling mean that the anisotropy of intralayer magnetic interactions differs in the MPS_3 materials. $MnPS_3$ appears to have Heisenberg spin interactions, $NiPS_3$ shows a weak and $CoPS_3$ a stronger easy-plane (XY) anisotropy, and $FePS_3$ has a strong Ising anisotropy [13,20–25]. Upon cooling, they all order in an AFM pattern, with respective transition temperatures T_N of 78, 118, 122, and 155 K for $MnPS_3$, $FePS_3$, $CoPS_3$ and $NiPS_3$ [11,16,26].

The weak van der Waals interlayer coupling leads to a cleavage energy close to that of graphite, and thus the MPS_3 materials are easy to exfoliate. Multiple efforts to thin MPS_3 samples have shown them to remain structurally stable down to a single layer [15,27]. Recent Raman scattering studies of monolayer $FePS_3$ have reported that T_N either drops from 117 to 104 K [28] or remains unchanged [24], which raises the possibility of substrate effects on this 2D Ising magnet [29]. Raman investigation of monolayer $NiPS_3$ indicates a suppression of long-range order relative to the bulk material, which was interpreted in the framework of the Berezinskii-Kosterlitz-Thouless (BKT) phase transition [30].

An alternative approach to dimensionality reduction is the incorporation of organic cations as spacers in the bulk materials, such that the altered layer separation enables control over the interlayer interactions [31,32]. This is complementary to electrochemical treatments with ionic liquids whose primary effect is to induce protonation, or other electron doping effects, when the sample is placed on the cathode side [33,34]. It was reported in the early literature that pyridine (C_5H_5N) can be intercalated into $MnPS_3$, leading to a transition from an AFM to a weakly FM ground state [2], and that the intercalation of alkylamines ($C_nH_{2n+1}NH_2$) into $FePS_3$ causes a strong reduction of T_N [3]. Much more recently, the intercalation of tetraheptylammonium-bromide ($C_{28}H_{60}BrN$) into $NiPS_3$ was found to cause a transition from AFM to ferrimagnetic (FIM) order, followed by another transition to AFM order, in effects ascribed to the electron doping of the layers [35].

In this work, we report the successful interlayer intercalation of $EMIM^+$ into $FePS_3$ and $NiPS_3$, using the ionic liquid $C_6H_{11}N_2BF_4$ (EMIM-BF_4). By measuring changes in the mass and interlayer spacing, we estimate the intercalation levels to be approximately 0.27 $EMIM^+$/f.u. in $FePS_3$ and 0.37 $EMIM^+$/f.u. in $NiPS_3$, and that both procedures dilate the c-axis lattice parameter by over 50%. We investigated the magnetic properties of $EMIM_x$-$FePS_3$ and $EMIM_x$-$NiPS_3$, and compared them with $FePS_3$ and $NiPS_3$, by magnetic susceptibility and ^{31}P nuclear magnetic resonance (NMR) measurements. We found that intercalation in $FePS_3$ causes changes in the Curie-Weiss temperatures determined above T_N, a suppression of T_N itself, and a reduced spin gap at the lowest temperatures. For intercalated $NiPS_3$, the magnetic transition temperature barely changes and the spin fluctuations become very isotropic, suggesting an evolution from weakly XY toward Heisenberg-type magnetism. Taken together with a dramatic suppression of any interlayer magnetic interactions, these data provide strong evidence for the systematic modulation of intralayer magnetic interactions by intercalation, for which we deduce that charge doping on the P site should be taken into account.

The structure of this article is as follows. In Sec. II, we describe our MPS_3 samples and intercalation procedure, and in Sec. III report our structural characterization. Section IV reports our measurements of the magnetic properties of pure and intercalated $FePS_3$ and Sec. V our data for pure and intercalated $NiPS_3$. In Sec. VI, we discuss the consequences of our results for the understanding of magnetism in MPS_3 materials and provide a brief conclusion.

II. MATERIALS AND METHODS

Single crystals of $FePS_3$ and $NiPS_3$ were grown by the method of chemical vapor transport (CVT) [26]. As Fig. 1(a) shows, the MPS_3 layer is composed of covalently bonded MS_6 octahedra and double-cone $[P_2S_6]^{4-}$ units in a 2:1 ratio

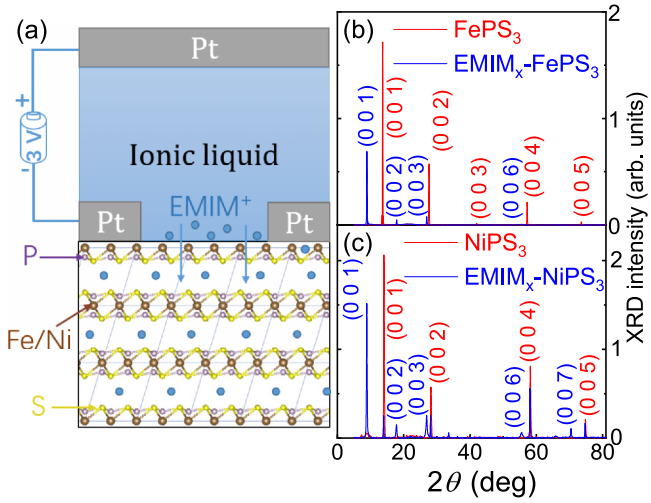

FIG. 2. Sample intercalation and structural characterization of $FePS_3$ and $NiPS_3$. (a) Configuration for electrochemical treatment with EMIM-BF_4. Two platinum electrodes are placed in the ionic liquid, set to a potential difference of 3 V, and the sample is attached to the negative electrode. (b) Single-crystal XRD data for $FePS_3$ and $EMIM_x$-$FePS_3$. (c) Single-crystal XRD data for $NiPS_3$ and $EMIM_x$-$NiPS_3$.

[36]. The M ions are thought to be in a robustly divalent M^{2+} state in all compounds, as shown for $FePS_3$ by x-ray photoelectron spectroscopy (XPS) [37]. These ions form the honeycomb lattice, with the P-P pairs located at the centers of the M hexagons [11,13,26]. The S^{2-} layers stack in an ABC configuration along the c direction to form a monoclinic structure with space group C2/m [12].

Both $FePS_3$ and $NiPS_3$ order magnetically with a "zigzag" pattern, as shown in Fig. 1(b). The Fe^{2+} ions in $FePS_3$ take their high-spin, $S = 2$ state and order with the moments normal to the ab plane [13]. These moments have FM alignment parallel to the a axis and AFM alignment along the b and c axes, with propagation wave vector $\boldsymbol{k} = [0\,1\,\frac{1}{2}]$ [20,23,38–41]. For $NiPS_3$, the Ni^{2+} ($S = 1$) moments are oriented primarily along the a axis with a small component perpendicular to the ab plane; the zigzag chains also lie along the a axis, with AFM alignment along b but an FM repeat along the c axis, resulting in $\boldsymbol{k} = [0\,1\,0]$ [20,42–44].

Figure 2(a) shows the configuration that we adopt for electrochemical treatment in order to achieve interlayer intercalation. The ionic liquid EMIM-BF_4 was packed in a container with two platinum electrodes placed approximately 20 mm apart and subjected to a 3 V potential difference [33,34]. A single crystal of $FePS_3$ or $NiPS_3$ was attached to the cathode and covered with silver paint. The ionic liquid was heated to a temperature around 60 °C. After 24 hours the mass of the samples had changed significantly, but longer treatment times led to no further change, and so one could declare the intercalation process to be complete.

X-ray diffraction (XRD) measurements were performed using Cu_α and Cu_β radiation to determine the c-axis lattice parameters. The d.c. magnetic susceptibility was measured in a Magnetic Property Measurement System (MPMS) with a field of 100 Oe and at temperatures down to 1.8 K in field-cooled (FC) and zero-field-cooled (ZFC) conditions. ^{31}P has nuclear spin $I = 1/2$ and a Zeeman factor of $^{31}\gamma = 17.235$ MHz/T. The ^{31}P NMR measurements were performed on single crystals using a top tuning circuit and the spectra collected by spin-echo pulse sequences. For broad spectra, frequency sweeps were used to acquire the full spectrum. NMR Knight shifts were calculated from $K_n = (f/^{31}\gamma H - 1)\times 100\%$, where f is the resonance frequency of the spectral peaks in the paramagnetic phase and the average frequency in the ordered phase. Spin-lattice relaxation rates, $1/^{31}T_1$, were measured by the standard magnetization inversion-recovery method. These constitute a sensitive probe of low-energy spin fluctuations, because $1/T_1T = \lim_{\omega\to 0}\Sigma_q A^2_{\rm hf}(q)\,{\rm Im}\,\chi(q,\omega)/\omega$, where $\chi(q,\omega)$ is the dynamical susceptibility, $A_{\rm hf}(q)$ is the hyperfine coupling, and ω is the NMR measurement frequency, which for electronic spins lies in the zero-energy limit.

TABLE I. c-axis lattice parameters of $FePS_3$, $EMIM_x$-$FePS_3$, $NiPS_3$, and $EMIM_x$-$NiPS_3$, and the estimated doping, x.

	$FePS_3$	$EMIM_x$-$FePS_3$	$NiPS_3$	$EMIM_x$-$NiPS_3$
c (Å)	6.723(1)	10.401(1)	6.642(1)	10.343(1)
x	0	$27 \pm 3\%$	0	$37 \pm 0.4\%$

III. LATTICE STRUCTURE AND DOPING OF $EMIM_x$-$FePS_3$ AND $EMIM_x$-$NiPS_3$

Figure 2(b) shows single-crystal XRD data for our $FePS_3$ samples before and after 24-hour electrochemical treatment with the ionic liquid EMIM-BF_4, and Fig. 2(c) the analogous data for $NiPS_3$. We focus on the (0 0 L) Bragg peaks in order to extract the interlayer (c-axis) dimension of the unit cell. Studying the intralayer structure, meaning the a and b parameters, requires powder XRD measurements, but it has been found that the grinding process introduces disorder within the layers that precludes a meaningful analysis. The positions of the (0 0 L) XRD peaks change appreciably after the intercalation treatment, and the c-axis lattice parameters are shown and compared in Table I. The c-axis dimension increases from 6.72 to 10.40 Å for $FePS_3$ and from 6.64 to 10.34 Å for $NiPS_3$. Such an extremely large (over 50%) increase in interlayer spacing can be expected to have a very strong effect on reducing the dimensionality to the 2D limit.

Because the sample is attached to the cathode, and because of the large change in c-axis parameter, we deduce that $EMIM^+$, rather than H^+, is intercalated into the materials. A similar observation of intercalation by a large organic molecule has also been reported in $NiPS_3$ using a different type of ionic liquid [35]. We note that our intercalation in $EMIM_x$-$NiPS_3$ was not complete by volume, in that a small portion of the XRD pattern of $EMIM_x$-$NiPS_3$ coincided with that of pristine $NiPS_3$ [visible in Fig. 2(c)]. However, the volume ratio of residual $NiPS_3$ is rather small, as we establish later from the absence of detectable signals in the magnetic susceptibility and NMR spectra.

The mass of the $FePS_3$ crystal increased from 0.18 ± 0.01 mg before to 0.21 ± 0.01 mg after intercalation. From this we

estimate the intercalant concentration and the charge doping level to be $x = 27 \pm 3\%$, given the molecular mass of 183 g/mol for $FePS_3$ and 111 g/mol for $EMIM^+$. For the $NiPS_3$ crystal, the mass changed from 3.86 ± 0.01 to 4.71 ± 0.01 mg, and thus we extracted the doping level as $x = 37 \pm 0.4\%$, using the molecular mass of 186 g/mol for $NiPS_3$. As part of our investigation we also performed ^{19}F NMR studies of the intercalated samples, which revealed in addition the presence of F^- ions (data not shown), suggesting an unknown small concentration of BF_4^- intercalants. The presence of BF_4^- in the $EMIM_x$-$FePS_3$ and $EMIM_x$-$NiPS_3$ samples need not be identical, and constitutes an additional possible source of error in the determination of x (for which we assumed that $EMIM^+$ doping was the only source of mass change). However, because our electrochemical setup [Fig. 2(a)] favors cationic intercalation, we expect this BF_4^- content to be small.

In summary, the fact that the lattice parameters of $FePS_3$ and $NiPS_3$ are very similar [12] does suggest that the ionic concentration x should be the same in both compounds after full intercalation. The concentrations we achieve are certainly similar, particularly when the uncertainties in their determination are taken into account, but one cannot exclude that small electrostatic differences between the two systems may give rise to a nontrivial difference in final x values.

IV. EXPERIMENTAL DATA ON $FePS_3$ AND $EMIM_x$-$FePS_3$

A. Magnetic susceptibility

Our susceptibility measurements were conducted on single crystals of $FePS_3$ and $EMIM_x$-$FePS_3$ with a small field applied parallel and perpendicular to the crystalline *ab* plane, and data under FC and ZFC conditions are shown in Fig. 3. In both pure and intercalated $FePS_3$, $\chi(T)$ is much bigger at temperatures above T_N when the field is perpendicular to the *ab* plane than when it lies in the *ab* plane, but much smaller below T_N. Such an anisotropy should indicate the Ising nature of the system, which is attributed to combination of trigonal distortion and spin-orbit coupling [13,21,22,45]. With $H \perp ab$, χ does not reach zero in the zero-temperature limit, which may be the consequence of a small field misalignment.

On cooling in $FePS_3$ [Fig. 3(a)], $\chi(T)$ exhibits a peak followed by a sharp drop at 120 K in both field orientations, indicating the Néel transition at $T_N \simeq 120$ K as found in previous reports [11,13,46]. There is no appreciable hysteresis with FC and ZFC conditions, which supports a second-order AFM transition, in contrast to earlier reports that this transition may be of first order [47,48]. Turning to $EMIM_x$-$FePS_3$, T_N taken from the peak position in $\chi(T)$ is reduced to 80 K by intercalation [Fig. 3(c)], which is a value still 2/3 of that in the pristine sample. These values of T_N will be verified by the NMR measurements to follow, and already contain one of our primary results, that there is little to no connection between T_N and a hypothetical interlayer coupling. The FC and ZFC data for $EMIM_x$-$FePS_3$ already differ at temperatures above T_N, but this difference is affected only minimally by the onset of magnetic order at T_N; thus we believe that the difference between the FC and ZFC datasets is not an intrinsic effect, but an extrinsic one caused by impurities that enter the sample during chemical intercalation.

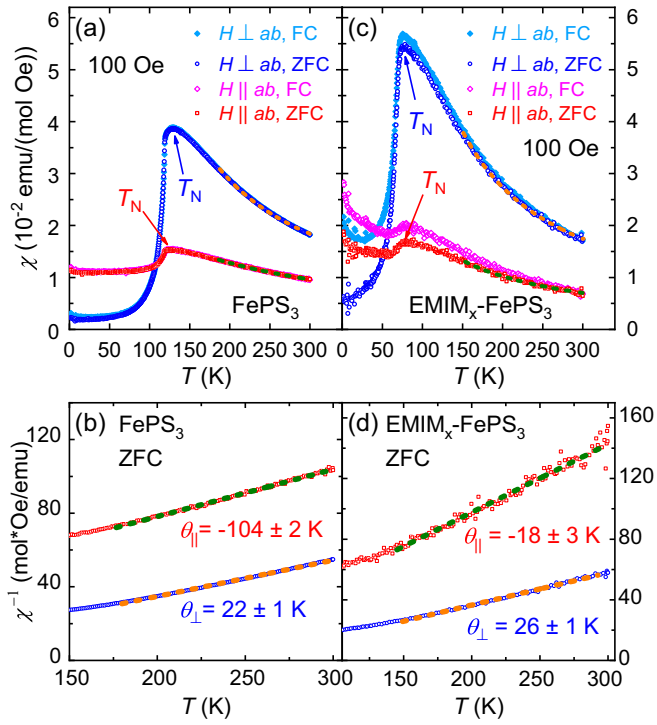

FIG. 3. Magnetic susceptibility of $FePS_3$ and $EMIM_x$-$FePS_3$. $\chi(T)$ measured in a field of 100 Oe applied parallel and perpendicular to the *ab* plane, under ZFC and FC conditions. (a) Susceptibility of $FePS_3$ shown as a function of temperature. (b) $1/\chi(T)$ of $FePS_3$ in the high-temperature PM phase. (c) Susceptibility of $EMIM_x$-$FePS_3$ shown as a function of temperature. (d) $1/\chi(T)$ of $EMIM_x$-$FePS_3$ in the high-temperature PM phase. T_N in (a) and (c) labels the AFM transition temperature, which is located at the peak of $\chi(T)$. Solid lines in (b) and (d) are linear fits to the data made over the temperature range shown, with θ obtained from the intercept on the x axis (i.e., at $y = 0$).

In all cases shown in Fig. 3, $\chi(T)$ above T_N can be well fitted by the Curie-Weiss (CW) form, $\chi = \frac{N\mu_0\mu_{\rm eff}^2}{3k_B(T-\theta)}$, where $\mu_{\rm eff}$ is the effective paramagnetic (PM) moment and θ is the CW temperature. In $FePS_3$ [Fig. 3(b)], the CW temperatures are found to be $\theta_\perp = 22 \pm 1$ K and $\theta_\parallel = -104 \pm 2$ K for the two field orientations. In our convention, the positive $\theta_\perp$ indicates the presence of FM interactions, as one may expect from the zigzag ground-state order; nevertheless, this ordered state is dominated by AFM interactions and by the Ising anisotropy, so our result reflects the magnetic frustration in the system. The CW fit to the perpendicular-field data returns a PM moment $\mu_{\rm eff} = 6.4 \pm 0.2\mu_B$/Fe, which is close to the literature value [13]; as noted in early studies, such a large $\mu_{\rm eff}$ for divalent Fe^{2+} ions can be explained only by taking the spin-orbit coupling into account [13].

For $EMIM_x$-$FePS_3$, the susceptibility shows the same type of anisotropy as the pristine sample [Fig. 3(c)]. The PM moments we extract, $6.0 \pm 0.2\mu_B$/Fe, are largely unaltered, indicating that intercalation causes no significant changes to the ionic properties. The CW temperatures we obtain, $\theta_\perp = 26 \pm 1$ K and $\theta_\parallel = -18 \pm 3$ K [Fig. 3(d)], suggest that no dramatic changes take place in the signs or energy scales of the couplings, but offer no straightforward interpretation as

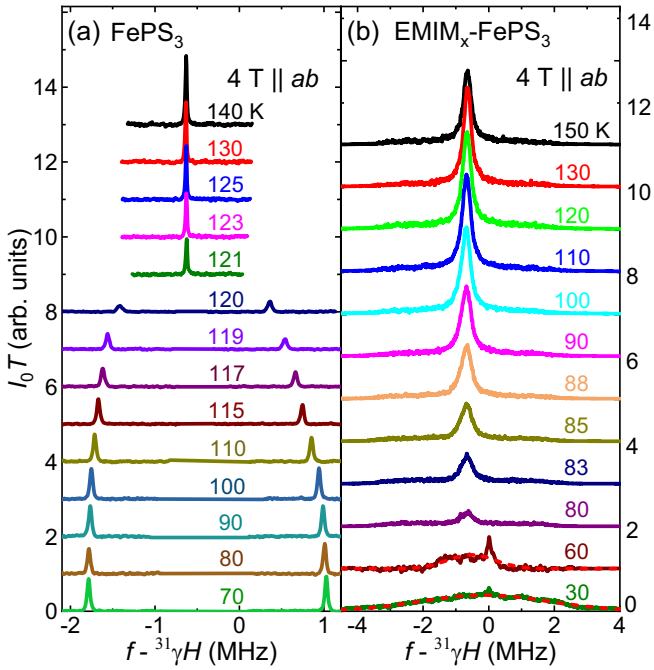

FIG. 4. ^{31}P NMR spectra of $FePS_3$ and $EMIM_x$-$FePS_3$. (a) Spectra of $FePS_3$ over a range of temperatures above and below T_N, taken at a fixed in-plane field of 4 T. Successive datasets are offset vertically for clarity. (b) Spectra of $EMIM_x$-$FePS_3$ taken under the same conditions. The spectral intensities at 30 and 60 K are multiplied by a factor of two; dashed lines represent Gaussian fits to the data.

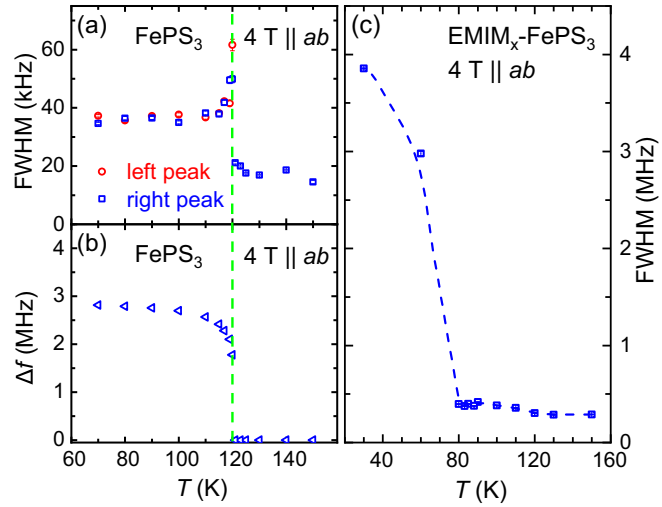

FIG. 5. NMR line widths and splittings in $FePS_3$ and $EMIM_x$-$FePS_3$. (a) FWHM of the primary spectral peak, or peaks, in $FePS_3$ [Fig. 4(a)] shown as a function of temperature. (b) Splitting, Δf, of NMR peaks in $FePS_3$ as a function of temperature. (c) FWHM of the broad NMR spectrum of $EMIM_x$-$FePS_3$ [Fig. 4(b)] shown as a function of temperature.

alterations to the dominant AFM or frustrating FM interactions. Because the susceptibility measurements contain significant impurity contributions whose subtraction is difficult to benchmark, we turn next from a bulk to a microscopic probe in order to gain deeper insight into the magnetic properties after intercalation.

B. NMR spectra

We measured ^{31}P NMR spectra for $FePS_3$ and $EMIM_x$-$FePS_3$ over a wide range of temperatures on both sides of T_N, and show our results in Fig. 4. In $FePS_3$, the single NMR peak observed at temperatures above 120 K splits into two nearly symmetrical peaks, presenting a clear signature of AFM ordering at T_N [Fig. 4(a)]. We note here that the field was applied in the *ab* plane, where from Fig. 1(b) one expects the ^{31}P nucleus to experience hyperfine fields from the two different sites that are in opposite directions relative to the external field. We then fitted the peak or peaks in each NMR spectrum with Gaussian profiles to extract the full width at half maximum height (FWHM) and the peak splitting below T_N. As Fig. 5(a) shows, the single NMR peak above 120 K broadens rapidly at T_N, from approximately 18 to over 50 kHz where it splits. The line splitting, Δf, approaches 2.8 MHz at low temperatures and, as shown in Fig. 5(b), from its shape can serve as an order parameter for the AFM phase.

For $EMIM_x$-$FePS_3$, the single NMR peak remains rather narrow when cooled down to 80 K [Fig. 4(b)]. Here it shows no evidence of a line splitting, but instead undergoes a large increase in line width [Fig. 5(c)]. This broadening can be taken to indicate the onset of magnetic order at $T_N \simeq 80$ K, consistent with the susceptibility data of Fig. 3, and Gaussian peak fits show the FWHM broadening from 300 kHz above T_N to 3 MHz below T_N. We draw attention to the fact that the low-temperature FWHM in $EMIM_x$-$FePS_3$ has the same order as Δf in $FePS_3$, which suggests a distribution of ordered moments in the system. Because we observe only one peak, we propose that these results reflect an incommensurate magnetic order in the 2D layers, with a systematic distribution of local-moment magnitudes and/or directions, as opposed to a multi-domain structure. Such an incommensurate order could arise from rather small alterations of the intralayer interactions in $FePS_3$, whose pre-intercalation compromise configuration is the Ising zigzag order shown in Fig. 1(b).

C. Spin-lattice relaxation rates and spin gaps

The spin-lattice relaxation rates, $1/^{31}T_1$, of pure and intercalated $FePS_3$ are shown in Fig. 6. $FePS_3$ exhibits the characteristic behavior on decreasing temperature that $1/^{31}T_1$ first increases to a maximum at $T = 120$ K, which reflects the AFM transition at T_N, followed by a rapid drop [Fig. 6(a)]. Far below T_N, the exponential fall suggests the form $1/^{31}T_1 \propto e^{-\Delta/k_BT}$, where Δ is the spin gap expected in an ordered Ising magnet. Plotting $\ln(1/^{31}T_1)$ as a function of $1/T$ reveals that the data below 50 K follow a straight line [Fig. 6(b)], whose gradient gives a gap $\Delta = 45 \pm 3$ K. Here we comment that inelastic neutron scattering (INS) measurements of the anisotropic spin-wave spectra have reported a gap of 15 meV [39], which is significantly larger than our NMR value. Because the NMR $1/T_1$ is a very sensitive, low-energy local probe that sums contributions from all of momentum space, it is possible that our results reveal a process missed by both triple-axis and time-of-flight INS for reasons of energy resolution or reciprocal-space coverage. However, the higher

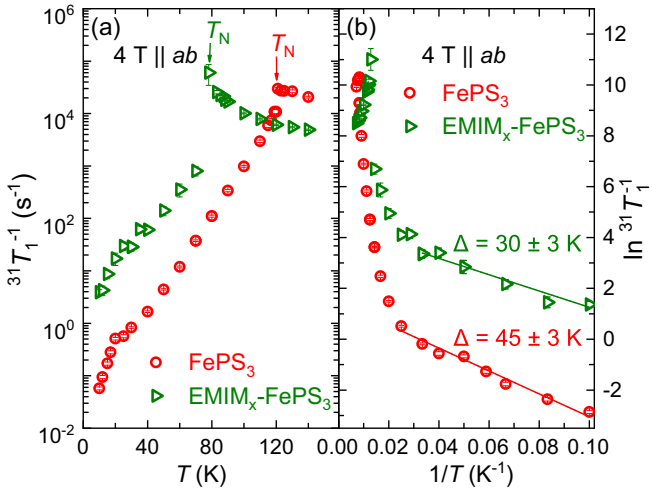

FIG. 6. Spin-lattice relaxation rates of $FePS_3$ and $EMIM_x$-$FePS_3$. (a) $1/^{31}T_1$ shown as a function of temperature, measured with an in-plane field of 4 T. (b) $1/^{31}T_1$ shown in semilog form as a function of $1/T$. The straight solid lines represent linear fits to the data in the low-temperature regime. Δ is a gap value extracted from the gradient of each line.

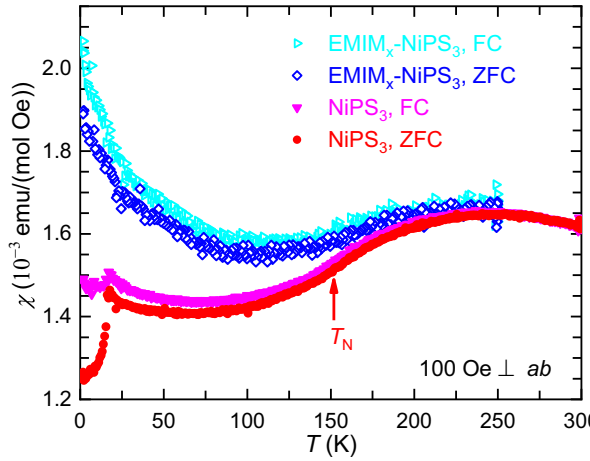

FIG. 7. Magnetic susceptibility of $NiPS_3$ and $EMIM_x$-$NiPS_3$. $\chi(T)$ measured in an out-of-plane field of 100 Oe under FC and ZFC conditions.

temperatures at which we obtained an NMR signal do leave open the possibility of probing a finite-energy transition, and we note also that T_1 becomes very long at these low temperatures, making the NMR $1/T_1$ measurement more sensitive to the presence of impurities. We hope that future studies may resolve this apparent contradiction.

Similar magnetic ordering and spin-gap behavior are observed in $EMIM_x$-$FePS_3$, as Fig. 6(a) shows. Here T_N is determined quite precisely at 78 K from the sharp peak in $1/^{31}T_1$. Analysis of the low-temperature response, shown in Fig. 6(b), gives the equivalent spin gap as $\Delta = 30 \pm 3$ K. This suppression of the gap upon intercalation scales linearly with the suppression of T_N, which would be consistent with a straightforward reduction of the relevant intralayer energies.

V. EXPERIMENTAL DATA ON $NiPS_3$ AND $EMIM_x$-$NiPS_3$

A. Magnetic susceptibility

The magnetic susceptibilities of $NiPS_3$ and $EMIM_x$-$NiPS_3$ are shown in Fig. 7. For both compounds, the peak in $\chi(T)$ occurs around 250 K, which makes it impossible to reach a high-temperature regime in which to extract the CW behavior. Such high intralayer energy scales are found by high-precision INS measurements of the spin dynamics of $NiPS_3$ [44], and the broad peak in χ indicates the development of 2D AFM correlations. We note that the AFM ordering transition is essentially invisible in $\chi(T)$, and we will show by NMR that $T_N = 148$ K (below). Detailed measurements on $NiPS_3$ showed that the susceptibility is isotropic above T_N and anisotropic below it [42]. The most notable feature in our measurements (Fig. 7) is the onset of a large difference between the FC and ZFC data below 25 K; because we found this downturn at different temperatures in different samples, we deduce that it is caused by quenched disorder and is not an intrinsic property.

For $EMIM_x$-$NiPS_3$, $\chi(T)$ is remarkably similar to the pristine compound, with only a small deviation setting in at temperatures below 200 K. This minimal alteration despite the massive increase in interlayer spacing is a strong indication that all the magnetic properties of $NiPS_3$ are intrinsically 2D. For the intercalated system, a difference between the ZFC and FC data develops gradually with decreasing temperature, unaffected by the onset of magnetic order (shown below by NMR), and we believe this to be a consequence of impurities introduced by the intercalation, similar to the situation in $EMIM_x$-$FePS_3$ (Fig. 3).

B. NMR spectra

Figure 8 shows the ^{31}P NMR spectra of $NiPS_3$ and $EMIM_x$-$NiPS_3$ over a wide range of temperature for both field orientations. For $NiPS_3$ in an out-of-plane field, the spectra above 148 K have a single peak characteristic of the PM phase, which broadens significantly on further cooling from 148 K to 140 K [Fig. 8(a)]. By contrast, the double-peak feature developing at all temperatures below 148 K in an in-plane field demonstrates clearly the onset of AFM order and fixes $T_N = 148 \pm 2$ K. In this case, Lorentzian functions gave a slightly better fit to the spectra, although this choice made little difference for the purpose of extracting the FWHM of each peak and the line splitting, Δf, below T_N [shown in Figs. 9(a) and 9(b)]. The FWHM is about 40 kHz at temperatures above T_N and saturates around 0.2 MHz far below T_N, while Δf also tends to level off around 0.2 MHz at low temperatures in the ordered state.

For $EMIM_x$-$NiPS_3$ in both field orientations, the NMR peaks also broaden significantly towards low temperatures [Figs. 8(c) and 8(d)]. Focusing first on high temperatures, as in $EMIM_x$-$FePS_3$ we did not, within the uncertainties imposed by the peak widths, resolve an average shift of the primary peak positions arising from chemical intercalation. In contrast to $EMIM_x$-$FePS_3$, however, we find that the spectra at and above 150 K exhibit an asymmetric shape that we capture by fitting each spectrum to a double-Lorentzian form. This procedure resolves a smaller second peak on the low-frequency

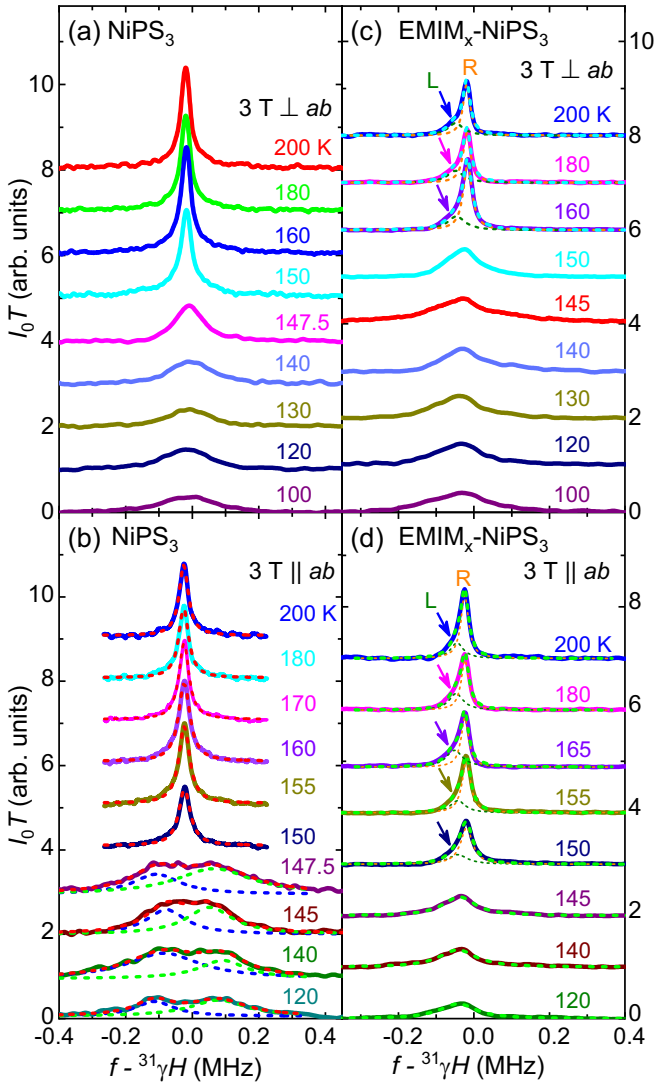

FIG. 8. ^{31}P NMR spectra of $NiPS_3$ and $EMIM_x$-$NiPS_3$. (a) Spectra of $NiPS_3$ measured in an out-of-plane field of 3 T over a wide range of temperatures above and below T_N. Successive datasets are offset vertically for clarity. (b) As in (a) with an in-plane field. The low-temperature spectra are fitted to a double-Lorentzian form. [(c) and (d)] Spectra of $EMIM_x$-$NiPS_3$ measured under the same conditions of field and temperature. Asymmetric peaks at and above 150 K are fitted to a double Lorentzian (short-dashed lines, marked by L and R, respectively), revealing a subdominant second contribution to the left of the main peak whose position is marked with an arrow.

side, marked by the arrows in Figs. 8(c) and 8(d), whose presence suggests a differential charge localization on the P sites that we discuss in Sec. VI. Below 150 K, we did not find a meaningful two-peak fit, instead using fits to a single Lorentzian to extract the FWHM, and Fig. 9(c) summarizes the data obtained with in-plane fields. The sudden increase in FWHM occurring at 145 K, which we label T^*, is characteristic of a static magnetic order. However, the absence of discernible line splitting at any lower temperatures suggests that this order could be of a type different from that in pristine $NiPS_3$.

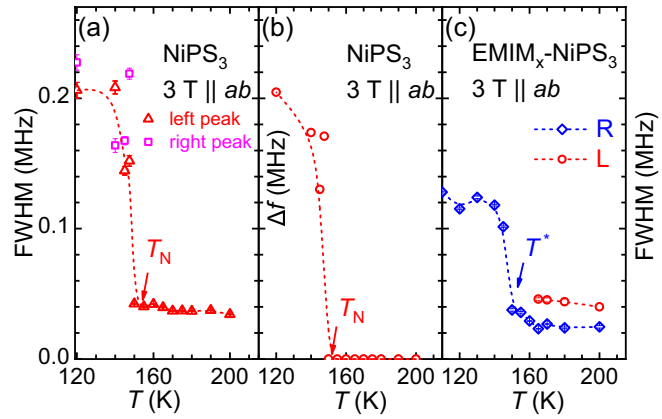

FIG. 9. NMR line widths and splittings in $NiPS_3$ and $EMIM_x$-$NiPS_3$. (a) FWHM of the primary spectral peak, or peaks, in $NiPS_3$ [Figs. 8(b)] shown as a function of temperature. (b) Splitting Δf of NMR peaks in $NiPS_3$ as a function of temperature. (c) FWHM of the broad NMR spectrum of $EMIM_x$-$NiPS_3$ [Figs. 8(d)] shown as a function of temperature. The arrows mark the transition temperatures, T_N and T^*, extracted for the two compounds.

C. Spin-lattice relaxation rates

The spin-lattice relaxation rates of $NiPS_3$ and $EMIM_x$-$NiPS_3$, measured in both field orientations, are presented in Fig. 10. We comment that it was not possible to obtain a reliable $1/^{31}T_1$ signal at temperatures significantly below 100 K, in contrast to the situation in $FePS_3$ (Fig. 6), but our data characterize well the magnetic transitions in both materials, which are clearly evident from the kinks in $1/^{31}T_1$. For $NiPS_3$ in both orientations, the rapid drop in $1/^{31}T_1$ determines precisely the AFM ordering temperature $T_N = 148$ K, a value slightly lower than that obtained from early susceptibility data [11,13,49]. Below T_N, $1/^{31}T_1$ for an in-plane field drops significantly faster than with an out-of-plane field, which is consistent with XY magnetic

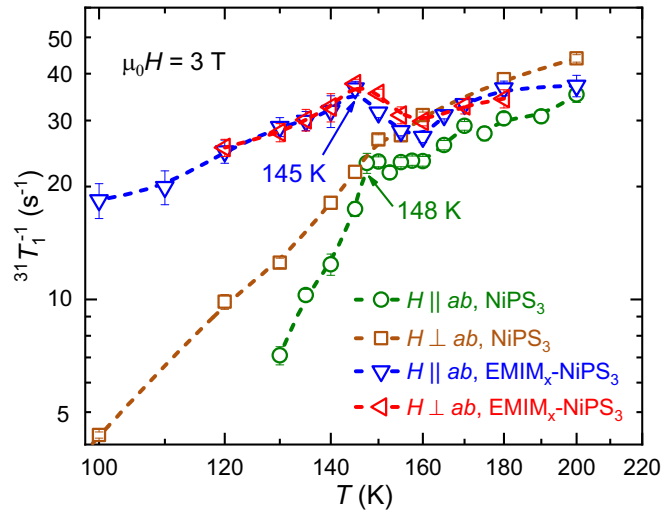

FIG. 10. Spin-lattice relaxation rates of $NiPS_3$ and $EMIM_x$-$NiPS_3$. $1/^{31}T_1$ shown as a function of temperature, measured with in- and out-of-plane fields of 3 T.

TABLE II. Magnetic interactions of $FePS_3$ and $NiPS_3$ [39,44]; J_i indicates a Heisenberg interaction between neighboring ions of differing separations [Fig. 1(b)] and D_z the leading magnetic anisotropy fitted by INS.

	J_1 (meV)	J_2 (meV)	J_3 (meV)	J' (meV)	D_z (meV)
$FePS_3$	−1.46	0.04	0.96	0.0073	−2.66
$NiPS_3$	−2.6	0.2	13.5	−0.3	0.21

order [50–52] in that the gapless (Goldstone) modes should be preserved only when the field is applied out of the plane.

For $EMIM_x$-$NiPS_3$, our $1/^{31}T_1$ data for the two field orientations are barely distinguishable above T^*, where they decrease with decreasing temperature from 200 to 160 K and then increase over the range from 160 to 145 K. Below this they drop more rapidly, allowing us to fix the putative magnetic ordering temperature as $T^* = 145$ K. Below T^*, the relaxation rates under in- and out-of-plane fields are truly indistinguishable, presenting the first of two distinctive contrasts between $NiPS_3$ and $EMIM_x$-$NiPS_3$. Such isotropic behavior suggests that intercalation in this system genuinely alters the intralayer magnetic interactions to a Heisenberg form. Second, although T^* is reduced by only 3 K on intercalation, $1/^{31}T_1$ at $T = 100$ K (far below T^*) is enhanced by a factor of five. This apparent strong enhancement of low-energy spin fluctuations points once again to the possibility of a magnetically ordered state different from that of pure $NiPS_3$ [Fig. 1(b)], candidates for which would include an incommensurate order. Further measurements are therefore required to investigate the magnetic structure of the intercalated system.

VI. DISCUSSION

Our susceptibility data indicate that the intercalation of $FePS_3$ and $NiPS_3$ does not cause any appreciable depletion of the available magnetic moments. Thus the changes we observe, specifically the reduction of T_N in $EMIM_x$-$FePS_3$ and the isotropic spin response of $EMIM_x$-$NiPS_3$, should be attributed to changes of the magnetic interactions. To discuss these, in Table II, we list the values of the magnetic interactions deduced by INS experiments for $FePS_3$ [39] and $NiPS_3$ [44]. The authors of both studies adopted a minimal model consisting of the three intralayer Heisenberg interactions illustrated in Fig. 1(b), an interlayer Heisenberg interaction (J'), and single-ion anisotropy terms, of which only one was found to be significant. The J' term was found to be very small in $FePS_3$ but potentially significant in $NiPS_3$. The J_3 term was found to be completely dominant in $NiPS_3$ and to play an essential role in establishing the zigzag order of $FePS_3$.

Considering the increase of the c-axis lattice parameter that we achieve, in excess of 50%, it is natural to expect that the interlayer couplings should be reduced dramatically. Thus our primary conclusion is that, beyond the role of their sign in establishing 3D order, the effective J' terms have no quantitative role in the magnetism of either material. The fact that magnetic order remains well established in $EMIM_x$-$FePS_3$ and essentially unaltered in $EMIM_x$-$NiPS_3$ points unequivocally to dominant 2D character. In the light of theoretical studies demonstrating that quasi-2D Heisenberg magnets with very small J' may nevertheless have significant T_N values [53], this result was not fully clear for $FePS_3$ (Table II). Our study demonstrates that it is also true for $NiPS_3$, despite the 3 K interlayer coupling scale extracted in Ref. [44].

It is then important to understand how the intralayer magnetic interactions are modified by intercalation. In principle, the addition of $EMIM^+$ should lead to electron doping in both materials, with the electrons presumably located on the M or P ions, and reaching a doping around $\frac{1}{3}e$/f.u. (0.27 in $EMIM_x$-$FePS_3$, 0.37 in $EMIM_x$-$NiPS_3$). The unchanged paramagnetic moments we extracted for $EMIM^+$-$FePS_3$ and the unchanged magnetic properties of $EMIM^+$-$NiPS_3$ seem to exclude a significant change of the M^{2+} valence. This suggests that the electronic doping should primarily affect the P sites, and indeed by transforming the less favorable P^{4+} configuration [37] to P^{3+}. In our results, the emergence of a second ^{31}P NMR peak at temperatures above 150 K in $EMIM_x$-$NiPS_3$, as shown in Figs. 8(c) and 8(d), supports charge doping and localization on the P sites, although it does not give immediate insight into the P valence. Here we note that, unlike in $FePS_3$ [37], XPS results for $NiPS_3$ report a strong coupling of the charge state to the spin order and a significant departure of the microscopic Ni valence state from 2+ [54], suggesting the involvement of the M ions in the details of valence shifts. Because magnetic quantities including the effective paramagnetic moment and spin-wave excitations tend to obey the nominal valence, a deeper analysis of this issue lies beyond the scope of our data. However, the fact that the P ions are located at the centers of the M hexagons should make P doping very effective in modifying the intralayer superexchange interactions, particularly the strong J_3 terms. We remark in this context that we found the intercalated samples to remain highly insulating, which is a prerequisite to regard the doped charges as localized, such that they can affect the magnetic interactions rather than drive a metallic transition.

Considering $FePS_3$ in more detail, the T_N we measure for bulk $EMIM_x$-$FePS_3$ is lower than the value $T_N = 104$ K obtained for monolayer $FePS_3$ [28]. Thus our intercalation is more than a simple isolation of the 2D units, and its effects on the competing intralayer interactions require more detailed microscopic modeling. In fitting their INS results, the authors of Ref. [39] assumed a rather minimal model where all of the anisotropy was ascribed to one single-ion term, and further anisotropic interactions such as Dzyaloshinskii-Moriya or Ising-type spin-spin interactions were neglected. The modeling of these terms is a complex task that was approached only recently by correlated density functional theory (DFT) methods [45], while further experimental information on the magnetic anisotropy has been obtained by x-ray photoelectron microscopy [55]. With the ongoing interest in $FePS_3$ as a candidate spintronic material [4], and for band engineering by ultrafast coherent light [56], a deeper understanding of the key interaction terms remains a priority.

In $EMIM_x$-$NiPS_3$, the fact that T^* is only 3 K lower than T_N in $NiPS_3$ demonstrates immediately the quantitative irrelevance of the J' terms. Nevertheless, the absence of discernible line splitting at low temperatures in the ^{31}P spectra of $EMIM_x$-$NiPS_3$ [Fig. 8(d)], in contrast to

the behavior in $NiPS_3$ [Fig. 8(b)], and the enhancement of $1/^{31}T_1$ (Fig. 10), lead us to suggest that the ordering at T^* may be of a different type, such as incomplete (short-ranged) or incommensurate. Recent theoretical work has indeed proposed that $NiPS_3$ is close to incommensurate magnetic order [57], and the large overlap of the two NMR peaks we observe in Fig. 8(b) may support this scenario. Another possibility could be weak anisotropy caused by intralayer strain arising from a lattice mismatch with the size of the intercalated molecules. Finally, a BKT transition is also possible if the system retains an easy-plane anisotropy, however weak, and in the intercalated system it is likely that quenched disorder would help to pin true long-range order from the quasi-long-ranged BKT order. We note here that a BKT phase has already been reported in monolayer $NiPS_3$ [30].

In summary, we performed electrochemical treatment of $FePS_3$ and $NiPS_3$ with the ionic liquid EMIM-BF_4, obtaining a significant intercalation of the large $EMIM^+$ ions into both compounds. The most important consequence of intercalation is a large and uniform increase of the c-axis lattice parameters, which unavoidably causes a strong reduction of interlayer couplings. The fact that we do not observe order-of-magnitude changes in the magnetic properties of either system demonstrates conclusively that the magnetic properties of the pristine materials are intrinsically 2D, being determined almost exclusively by intralayer physics. The changes we do observe are a consequence of modulated intralayer magnetic interactions. In $FePS_3$, the drop in magnetic ordering temperature suggests a change in the competing FM and AFM interactions while the system remains in the Ising limit; the effects in $NiPS_3$ are far more subtle, with the interactions changing from weakly XY-type to almost isotropic (Heisenberg-type). We propose the charge doping that accompanies intercalation, which appears to be localized around the P ions and reaches a level of 0.3–0.4 e^-/f.u., as the mechanism most likely to drive these changes. Our study of chemical intercalation with ionic liquids paves the way not only for approaching the 2D limit in van der Waals magnetic materials but also for tuning their intralayer magnetic interactions.

ACKNOWLEDGMENTS

This work was supported by the National Key R&D Program of China (under Grants No. 2023YFA1406500, No. 2022YFA1402700, No. 2023YFA1406100, and No. 2019YFA0308602), the National Natural Science Foundation of China (under Grants No. 12134020, No. 12374156, No. 12174441, and No. 12074425), the Fundamental Research Funds for the Central Universities, and the Research Funds of Renmin University of China (under Grants No. 22XNH096 and No. 23XNKJ22). Y. F. Guo acknowledges the Double First-Class Initiative Fund of ShanghaiTech University.

[1] H. Bethe, Zur Theorie der Metalle, Z. Physik **71**, 205 (1931).
[2] J. P. Alias and V. Sukumaran, The intercalation reaction of pyridine with manganese thiophosphate, $MnPS_3$, J. Am. Chem. Soc. **114**, 7792 (1992).
[3] A. J. Pattayil and V. Sukumaran, Intercalation of n-alkylamines in iron thiohypophosphate ($FePS_3$), Chem. Mater. **5**, 1182 (1993).
[4] A. Soumyanarayanan, N. Reyren, A. Fert, and C. Panagopoulos, Emergent phenomena induced by spin-orbit coupling at surfaces and interfaces, Nature (London) **539**, 509 (2016).
[5] K. S. Burch, D. Mandrus, and J.-G. Park, Magnetism in two-dimensional van der Waals materials, Nature (London) **563**, 47 (2018).
[6] C. Gong, L. Li, Z. L. Li, H. W. Ji, A. Stern, Y. Xia, T. Cao, W. Bao, C. Z. Wang, Y. Wang, Z. Q. Qiu, R. J. Cava, S. G. Louie, J. Xia, and X. Zhang, Discovery of intrinsic ferromagnetism in two-dimensional van der Waals crystals, Nature (London) **546**, 265 (2017).
[7] B. Huang, G. Clark, E. Navarro-Moratalla, D. R. Klein, R. Cheng, K. L. Seyler, D. Zhong, E. Schmidgall, M. A. McGuire, D. H. Cobden, W. Yao, D. Xiao, P. Jarillo-Herrero, and X. D. Xu, Layer-dependent ferromagnetism in a van der Waals crystal down to the monolayer limit, Nature (London) **546**, 270 (2017).
[8] Y. Tian, M. J. Gray, H. W. Ji, R. J. Cava, and K. S. Burch, Magneto-elastic coupling in a potential ferromagnetic 2D atomic crystal, 2D Mater. **3**, 025035 (2016).
[9] D. J. O'Hara, T. C. Zhu, A. H. Trout, A. S. Ahmed, Y. Q. K. Luo, C. H. Lee, M. R. Brenner, S. Rajan, J. A. Gupta, D. W. McComb, and R. K. Kawakami, Room temperature intrinsic ferromagnetism in epitaxial manganese selenide films in the monolayer limit, Nano Lett. **18**, 3125 (2018).
[10] M. Bonilla, S. Kolekar, Y. J. Ma, H. C. Diaz, V. Kalappattil, R. Das, T. Eggers, H. R. Gutierrez, M.-H. Phan, and M. Batzill, Strong room-temperature ferromagnetism in VSe_2 monolayers on van der Waals substrates, Nat. Nanotechnol. **13**, 289 (2018).
[11] G. Le Flem, R. Brec, G. Ouvard, A. Louisy, and P. Segransan, Magnetic interactions in the layer compounds MPX_3 (M = Mn, Fe, and Ni; X = S, Se), J. Phys. Chem. Solids **43**, 455 (1982).
[12] G. Ouvrard, R. Brec, and J. Rouxel, Structural determination of some MPS_3 layered phases (M = Mn, Fe, Co, Ni, and Cd), Mater. Res. Bull. **20**, 1181 (1985).
[13] P. A. Joy and S. Vasudevan, Magnetism in the layered transition-metal thiophosphates MPS_3 (M = Mn, Fe, and Ni), Phys. Rev. B **46**, 5425 (1992).
[14] B. L. Chittari, Y. Park, D. Lee, M. Han, A. H. MacDonald, E. Hwang, and J. Jung, Electronic and magnetic properties of single-layer MPX_3 metal phosphorous trichalcogenides, Phys. Rev. B **94**, 184428 (2016).
[15] K. Z. Du, X. Z. Wang, Y. Liu, P. Hu, M. I. B. Utama, C. K. Gan, Q. H. Xiong, and C. Kloc, Weak van der Waals stacking, wide-range band gap, and raman study on ultrathin layers of metal phosphorus trichalcogenides, ACS Nano **10**, 1738 (2016).
[16] F. M. Wang, T. A. Shifa, P. Yu, P. He, Y. Liu, F. Wang, Z. X. Wang, X. Y. Zhan, X. D. Lou, F. Xia, and J. He, New frontiers on van der Waals layered metal phosphorous trichalcogenides, Adv. Funct. Mater. **28**, 1802151 (2018).

[17] Z. Wang, M. Wang, J. Lehmann, Y. Shiomi, T.-h. Arima, N. Nagaosa, Y. Tokura, and N. Ogawa, Electric-field-enhanced second-harmonic domain contrast and nonreciprocity in a van der Waals antiferromagnet, arXiv:2401.11222.

[18] C. R. S. Haines, M. J. Coak, A. R. Wildes, G. I. Lampronti, C. Liu, P. Nahai-Williamson, H. Hamidov, D. Daisenberger, and S. S. Saxena, Pressure-induced electronic and structural phase evolution in the van der Waals compound $FePS_3$, Phys. Rev. Lett. **121**, 266801 (2018).

[19] S. Kang, K. Kim, B. H. Kim, J. Kim, K. I. Sim, J.-U. Lee, S. Lee, K. Park, S. Yun, T. Kim, A. Nag, A. Walters, M. Garcia-Fernandez, J. Li, L. Chapon, K.-J. Zhou, Y.-W. Son, J. H. Kim, H. Cheong, and J.-G. Park, Coherent many-body exciton in van der Waals antiferromagnet $NiPS_3$, Nature (London) **583**, 785 (2020).

[20] K. Kurosawa, S. Saito, and Y. Yamaguchi, Neutron diffraction study on $MnPS_3$ and $FePS_3$, J. Phys. Soc. Jpn. **52**, 3919 (1983).

[21] N. Chandrasekharan and S. Vasudevan, Magnetism, exchange and crystal field parameters in the orbitally unquenched Ising antiferromagnet $FePS_3$, Pramana **43**, 21 (1994).

[22] I. Chatterjee, Magnetic properties of layered antiferromagnets, Phys. Rev. B **51**, 3937 (1995).

[23] K. C. Rule, G. J. McIntyre, S. J. Kennedy, and T. J. Hicks, Single-crystal and powder neutron diffraction experiments on $FePS_3$: Search for the magnetic structure, Phys. Rev. B **76**, 134402 (2007).

[24] J. U. Lee, S. Lee, J. H. Ryoo, S. Kang, T. Y. Kim, P. Kim, C. H. Park, J. G. Park, and H. Cheong, Ising-type magnetic ordering in atomically thin $FePS_3$, Nano Lett. **16**, 7433 (2016).

[25] A. R. Wildes, V. Simonet, E. Ressouche, R. Ballou, and G. J. McIntyre, The magnetic properties and structure of the quasi-two-dimensional antiferromagnet $CoPS_3$, J. Phys.: Condens. Matter **29**, 455801 (2017).

[26] R. Brec, Review on structural and chemical properties of transition metal phosphorous trisulfides MPS_3, Solid State Ion. **22**, 3 (1986).

[27] C. T. Kuo, M. Neumann, K. Balamurugan, H. J. Park, S. Kang, H. W. Shiu, J. H. Kang, B. H. Hong, M. Han, T. W. Noh, and J.-G. Park, Exfoliation and Raman spectroscopic fingerprint of few-layer $NiPS_3$ van der Waals crystals, Sci. Rep. **6**, 20904 (2016).

[28] X. Z. Wang, K. Z. Du, Y. Y. F. Liu, P. Hu, J. Zhang, Q. Zhang, M. H. S. Owen, X. Lu, C.W. Gan, P. Sengupta, C. Kloc, and Q. H. Xiong, Raman spectroscopy of atomically thin two-dimensional magnetic iron phosphorus trisulfide ($FePS_3$) crystals, 2D Mater. **3**, 031009 (2016).

[29] A. McCreary, J. R. Simpson, T. T. Mai, R. D. McMichael, J. E. Douglas, N. Butch, C. Dennis, R. Valdés Aguilar, and A. R. Hight Walker, Quasi-two-dimensional magnon identification in antiferromagnetic $FePS_3$ via magneto-Raman spectroscopy, Phys. Rev. B **101**, 064416 (2020).

[30] L. L. Hu, H. X. Wang, Y. Z. Chen, K. Xu, M.-R. Li, H. Y. Liu, P. Gu, Y. B. Wang, M. D. Zhang, H. Yao, and Q. H. Xiong, Observation of a magnetic phase transition in monolayer $NiPS_3$, Phys. Rev. B **107**, L220407 (2023).

[31] H. X. Zhang, A. Rousuli, S. C. Shen, K. N. Zhang, C. Wang, L. P. Luo, J. Z. Wang, Y. Wu, Y. Xu, W. H. Duan, H. Yao, P. Yu, and S. Y. Zhou, Enhancement of superconductivity in organic-inorganic hybrid topological materials, Sci. Bull. **65**, 188 (2020).

[32] H. X. Zhang, A. Rousuli, K. N. Zhang, L. P. Luo, C. G. Guo, X. Cong, Z. Z. Lin, C. H. Bao, H. Y. Zhang, S. N. Xu, R. F. Feng, S. C. Shen, K. Zhao, W. Yao, Y. Wu, S. H. Ji, X. Chen, P. H. Tan, Q. K. Xue, Y. Xu, W. H. Duan, P. Yu, and S. Y. Zhou, Tailored Ising superconductivity in intercalated bulk $NbSe_2$, Nat. Phys. **18**, 1425 (2022).

[33] Y. Cui, G. H. Zhang, H. B. Li, H. Lin, X. Y. Zhu, H.-H. Wen, G. Q. Wang, J. Z. Sun, M. W. Ma, Y. Li, D. L. Gong, T. Xie, Y. H. Gu, S. L. Li, H. Q. Luo, P. Yu, and W.Q. Yu, Protonation induced high-t_c phases in iron-based superconductors evidenced by NMR and magnetization measurements, Sci. Bull. **63**, 11 (2018).

[34] Y. Cui, Z. Hu, J. S. Zhang, W. L. Ma, M. W. Ma, Z. Ma, C. Wang, J. Q. Yan, J. P. Sun, J. G. Cheng, S. Jia, Y. Li, J. S. Wen, H. C. Lei, P. Yu, W. Ji, and W. Q. Yu, Ionic-liquid-gating induced protonation and superconductivity in FeSe, $FeSe_{0.93}S_{0.07}$, ZrNCl, 1T -TaS_2 and $BiSe_2$, Chin. Phys. Lett. **36**, 077401 (2019).

[35] M. J. Mi, X. W. Zheng, S. L. Wang, Y. Zhou, L. X. Yu, H. Xiao, H. N. Song, B. Shen, F. S. Li, L. H. Bai, Y. X. Chen, S. P. Wang, X. H. Liu, and Y. L. Wang, Variation between antiferromagnetism and ferrimagnetism in $NiPS_3$ by electron doping, Adv. Funct. Mater. **32**, 2112750 (2022).

[36] R. Brec, G. Ouvrard, and J. Rouxel, Relationship between structure parameters and chemical properties in some MPS_3 layered phases, Mater. Res. Bull. **20**, 1257 (1985).

[37] Z. Yu, J. Peng, Y. H. Liu, W. X. Liu, H. F. Liu, and Y. Q. Guo, Amine-assisted exfoliation and electrical conductivity modulation toward few-layer $FePS_3$ nanosheets for efficient hydrogen evolution, J. Mater. Chem. A **7**, 13928 (2019).

[38] A. R. Wildes, K. C. Rule, R. I. Bewley, M. Enderle, and T. J. Hicks, The magnon dynamics and spin exchange parameters of $FePS_3$, J. Phys.: Condens. Matter **24**, 416004 (2012).

[39] D. Lançon, H. C. Walker, E. Ressouche, B. Ouladdiaf, K. C. Rule, G. J. McIntyre, T. J. Hicks, H. M. Rønnow, and A. R. Wildes, Magnetic structure and magnon dynamics of the quasi-two-dimensional antiferromagnet $FePS_3$, Phys. Rev. B **94**, 214407 (2016).

[40] M. J. Coak, D. M. Jarvis, H. Hamidov, A. R. Wildes, J. A. M. Paddison, C. Liu, C. R. S. Haines, N. T. Dang, S. E. Kichanov, B. N. Savenko, S. Lee, M. Kratochvílová, S. Klotz, T. C. Hansen, D. P. Kozlenko, J. G Park, and S. S. Saxena, Emergent magnetic phases in pressure-tuned van der Waals antiferromagnet $FePS_3$, Phys. Rev. X **11**, 011024 (2021).

[41] S. Paul, D. Negi, S. Talukdar, S. Karak, S. Badola, B. Poojitha, M. Mandal, S. Marik, R. P. Singh, N. Pistawala, L. Harnagea, A. Thomas, A. Soni, S. Bhattacharjee, and S. Saha, Tuning the magnetic properties in MPS_3 (M = Mn, Fe and Ni) by proximity-induced Dzyaloshinskii-Moriya interactions, arXiv:2307.13400.

[42] A. R. Wildes, V. Simonet, E. Ressouche, G. J. McIntyre, M. Avdeev, E. Suard, S. A. J. Kimber, D. Lançon, G. Pepe, B. Moubaraki, and T. J. Hicks, Magnetic structure of the quasi-two-dimensional antiferromagnet $NiPS_3$, Phys. Rev. B **92**, 224408 (2015).

[43] T. Y. Kim and C. H. Park, Magnetic anisotropy and magnetic ordering of transition-metal phosphorus trisulfides, Nano Lett. **21**, 10114 (2021).

[44] A. R. Wildes, J. R. Stewart, M. D. Le, R. A. Ewings, K. C. Rule, G. Deng, and K. Anand, Magnetic dynamics of $NiPS_3$, Phys. Rev. B **106**, 174422 (2022).

[45] M. Amirabbasi and P. Kratzer, Orbital and magnetic ordering in single-layer $FePS_3$: A DFT + U study, Phys. Rev. B **107**, 024401 (2023).

[46] K. Okuda, K. Kurosawa, and S. Saito, High field magnetization process in $FePS_3$, in *High Field Magnetism*, edited by M. Date (Elsevier, Amsterdam, 1983) pp. 55–58.

[47] P. Jernberg, S. Bjarman, and R. Wäppling, $FePS_3$: A first-order phase transition in 2DIsing antiferromagnet, J. Magn. Magn. Mater. **46**, 178 (1984).

[48] P. Ferloni and M. Scagliotti, Magnetic phase transitions in iron and nickel phosphorus trichalcogenides, Thermochim. Acta **139**, 197 (1989).

[49] J. Ziolo, S. Torre, A. Rigamonti, and F. Borsa, ^{31}P NMR relaxation study of spin dynamics in layered transition-metal compounds MPX_3, J. Appl. Phys. **63**, 3095 (1988).

[50] S. Rosenblum, A. H. Francis, and R. Merlin, Two-magnon light scattering in the layered antiferromagnet $NiPS_3$: Spin-1/2-like anomalies in a spin-1 system, Phys. Rev. B **49**, 4352 (1994).

[51] K. Kim, S. Y. Lim, J.-U. Lee, S. Lee, T. Y. Kim, K. Park, G. S. Jeon, C.-H. Park, J.-G. Park, and H. Cheong, Suppression of magnetic ordering in XXZ-type antiferromagnetic monolayer $NiPS_3$, Nat. Commun. **10**, 345 (2019).

[52] D. Jana, P. Kapuscinski, I. Mohelsky, D. Vaclavkova, I. Breslavetz, M. Orlita, C. Faugeras, and M. Potemski, Magnon gap excitations and spin-entangled optical transition in the van der Waals antiferromagnet $NiPS_3$, Phys. Rev. B **108**, 115149 (2023).

[53] C. Yasuda, S. Todo, K. Hukushima, F. Alet, M. Keller, M. Troyer, and H. Takayama, Néel temperature of quasi-low-dimensional Heisenberg antiferromagnets, Phys. Rev. Lett. **94**, 217201 (2005).

[54] S. Y. Kim, T. Y. Kim, L. J. Sandilands, S. Sinn, M.-C. Lee, J. Son, S. Lee, K.-Y. Choi, W. Kim, B.-G. Park, C. Jeon, H.-D. Kim, C.-H. Park, J.-G. Park, S. J. Moon, and T. W. Noh, Charge-spin correlation in van der Waals antiferromagnet $NiPS_3$, Phys. Rev. Lett. **120**, 136402 (2018).

[55] Y. Lee, S. Son, C. Kim, S. Kang, J. Shen, M. Kenzelmann, B. Delley, T. Savchenko, S. Parchenko, W. Na, K.-Y. Choi, W. Kim, H. Cheong, P. M. Derlet, A. Kleibert, and J.-G. Park, Giant magnetic anisotropy in the atomically thin van der Waals antiferromagnet $FePS_3$, Adv. Electron. Mater. **9**, 2200650 (2023).

[56] F. Mertens, D. Mönkebüscher, U. Parlak, C. Boix-Constant, S. Mañas-Valero, M. Matzer, R. Adhikari, A. Bonanni, E. Coronado, A. M. Kalashnikova, D. Bossini, and M. Cinchetti, Ultrafast coherent THz lattice dynamics coupled to spins in the van der Waals antiferromagnet $FePS_3$, Adv. Mater. **35**, 2208355 (2023).

[57] P. Mellado, Spin model for the honeycomb $NiPS_3$, Appl. Phys. Lett. **123**, 242403 (2023).